



CHORUS

This is the accepted manuscript made available via CHORUS. The article has been published as:

High- T_c superconductivity in weakly electron-doped HfNCI

Betül Pamuk, Francesco Mauri, and Matteo Calandra

Phys. Rev. B **96**, 024518 — Published 27 July 2017

DOI: [10.1103/PhysRevB.96.024518](https://doi.org/10.1103/PhysRevB.96.024518)

High T_c superconductivity in weakly electron-doped HfNCl

Betül Pamuk,^{1,2} Francesco Mauri,^{3,4,*} and Matteo Calandra^{1,†}

¹CNRS, UMR 7590 and Sorbonne Universités, UPMC Univ Paris 06, IMPMC - Institut de Minéralogie, de Physique des Matériaux, et de Cosmochimie, 4 place Jussieu, F-75005, Paris, France

²School of Applied and Engineering Physics, Cornell University, Ithaca, NY 14853, USA

³Dipartimento di Fisica, Università di Roma La Sapienza, Piazzale Aldo Moro 5, I-00185 Roma, Italy

⁴Graphene Labs, Fondazione Istituto Italiano di Tecnologia, Via Morego, I-16163 Genova, Italy

We investigate magnetic and superconducting properties in electron-doped Li_xHfNCl . HfNCl is a band insulator that undergoes an insulator to superconductor transition upon doping at $x \approx 0.13$. The persistence of the insulating state for $x < 0.13$ is due to an Anderson transition probably related to Li disorder. In the metallic and superconducting phase, Li_xHfNCl is a prototype two-dimensional two-valley electron gas with parabolic bands. By performing a model random phase approximation approach as well as first-principles range-separated HSE06 calculations, we find that the spin susceptibility χ_s is strongly enhanced in the low-doping regime by the electron-electron interaction. Furthermore, in the low-doping limit, the exchange interaction renormalizes the intervalley electron-phonon coupling and results in a strong increase of the superconducting critical temperature for $x < 0.15$. On the contrary, for $x > 0.15$, T_c is approximately constant, in agreement with experiments. At $x = 0.055$ we found that T_c can be as large as 40 K, suggesting that the synthesis of cleaner samples of Li_xHfNCl could remove the Anderson insulating state competing with superconductivity and generate a high T_c superconductor.

PACS numbers: 74.20.Pq, 74.62.Dh, 74.78.-w, 71.10.Ca

I. INTRODUCTION

The low-doping limit of multivalley semiconductors has recently been proposed as an alternative route to achieve high T_c superconductivity^{1–3}. Transition metal dichalcogenides^{4–7}, ternary transition-metal dinitrides⁸, and cloronitrides^{9,10} have been reported to achieve fairly high T_c upon doping. It is possible to dope multivalley semiconductors up to electron densities of $n \sim 10^{14} \text{ cm}^{-2}$ via field-effect doping^{1,4,5,11–13}. The doping of these materials can be also be achieved and controlled by intercalation^{9,10,14–17}. However, reaching the low-doping limit can be difficult as disorder and the consequent Anderson transition can suppress superconductivity.

In a two-dimensional, and quasi two-dimensional (2D) semiconductors, in the weakly-doped regime, the density of states (DOS) is constant. This is different from 3D semiconductors with parabolic bands, where generally the density of states increases as $\sqrt{\epsilon_F}$, as the number of electrons increases, ϵ_F being the Fermi level. Therefore, in 3D semiconductors, a large number of carriers is needed¹⁸ to achieve a sizeable density of states at the Fermi level $N(0)$. As in a phonon-mediated mechanism, $T_c \sim N(0)$, in a 2D semiconductor, T_c is expected to be constant because of the constant DOS, as long as the phonon spectrum is weakly affected by doping. However, in the weakly doped regime of transition-metal chloronitrides, the T_c increases with decreasing doping^{9,10,14}. This unexpected behavior resulted in a search for a theoretical understanding of the physics of superconductivity in 2D semiconductors^{19–26}.

In previous works, it has been shown that in 2D multivalley semiconductors, at low doping, the electron-

electron interaction enhances the intervalley electron-phonon coupling, explaining the behavior of T_c ^{25,26}. The enhancement of the T_c is linked to the enhancement of the spin susceptibility, χ_s . Furthermore, a systematic study of electronic, magnetic, and vibrational properties of Li_xZrNCl has been performed using density functional theory (DFT) with hybrid functionals with exact exchange and range separation, and this study shows that the exact exchange component leads to a similar enhancement in spin susceptibility and electron-phonon interaction²⁶. This effect on the enhancement of T_c should be quite general as it only requires basic general ingredients such as a 2D multivalley (ideally two-valley) semiconductor and large enough electron-gas parameter, $r_s = 1/a_B\sqrt{\pi n}$ with $a_B = \epsilon_M\hbar^2/(m^*e^2)$ where n is the electron density per unit area (linked to the doping per formula unit, x , per area Ω of 2 formula units for Li_xZrNCl : $n = 2x/\Omega$), ϵ_M is the environmental dielectric constant (i.e. the dielectric constant of the undoped semiconductor), and m^* the effective mass of the electronic band²⁵. Therefore, it is natural to search for high T_c superconductivity in other materials with either larger ϵ_M or with lower n and m^* .

An interesting system with these features can be intercalated HfNCl. Superconductivity has been observed with Li-intercalated β -HfNCl with $T_c = 20 \text{ K}$ ¹⁵, and with co-intercalated $\text{Li}_{0.48}(\text{THF})_y\text{HfNCl}$ with $T_c = 25.5 \text{ K}$ ^{10,15}. As β -ZrNCl, β -HfNCl is a two dimensional two-valley semiconductor with almost perfect parabolic conduction band and constant DOS. Moreover, in β -HfNCl, $\epsilon_M = 4.93$ ²¹ is slightly smaller than in the case of β -ZrNCl ($\epsilon_M = 5.59$). Thus, it is natural to expect that a similar enhancement in the T_c at low doping occurs also

in Li_xHfNCl . However, the T_c in Li_xHfNCl is surprisingly flat in the weakly-doped regime, and the Anderson transition occurs at almost three times larger doping ($x \approx 0.15$) with respect to Li_xZrNCl . It is then possible that the Anderson transition prevents the enhancement of the T_c at low doping, or alternatively, the reported doping is indeed nominal doping and not the real electron doping occurring in the sample. More experimental insight into the low-doping regime can also be obtained by field-effect doping. In this work, we follow the method introduced in References 25 and 26 to explore the behavior in Li_xHfNCl . We propose that clean samples at sufficiently low doping can achieve higher T_c without the need of further intercalation.

II. COMPUTATIONAL DETAILS

Calculations are performed using the QUANTUM ESPRESSO *ab initio* method²⁷ with the generalized gradient approximation (GGA) as implemented in the PBE functional²⁸ with ultrasoft norm conserving pseudopotentials and plane wave basis sets. The doping of the semiconductor is simulated by changing the number of electrons and adding a compensating jellium background, which has been previously shown to give accurate results^{20,24}. The atomic coordinates are relaxed with lattice parameters fixed at the experimental values from Reference 15. For the energy convergence, a threshold on the change in total energy of 10^{-10} Ry is used for all calculations. A Methfessel-Paxton smearing of 0.01 Ry with an electron-momentum grid of $48 \times 48 \times 48$ are used for the relaxation of the internal coordinates and calculating the electronic band structure. The density of states is calculated using a Gaussian smearing of 0.01 Ry.

Furthermore, we have performed calculations with the HSE06²⁹ functional that has exact exchange and range separation components, using the CRYSTAL code³⁰ with Gaussian type triple- ζ valence polarized basis set orbitals^{31,32} where the diffuse Gaussian functions of the Hf basis are reoptimized. A Fermi-Dirac smearing of 0.0025 Ha, electron-momentum grid of $48 \times 48 \times 16$, energy convergence threshold of 10^{-9} Ha, real space integration tolerances of 8-12-8-30-60, with 6th order multipolar expansion are used for the HSE06 calculations.

The effective mass, m^* is calculated from the curvature of a 4th order polynomial fit to the region between the Fermi energy and the conduction band minimum around the special point \mathbf{K} , assuming that the mass tensor is isotropic.

Electron-phonon coupling and phonon frequencies are calculated with the PBE functional with a Methfessel-Paxton smearing of 0.02 Ry, electron-momentum grid of $12 \times 12 \times 4$, Wannierization³³ of the electronic bands with an electron-momentum grid of $6 \times 6 \times 2$, correspondingly, a phonon-momentum grid of $6 \times 6 \times 2$, and a Wannier interpolation scheme of electron-phonon coupling with a grid of $40 \times 40 \times 6$ ³⁴.

III. RESULTS AND DISCUSSION

A. Electronic structure

The primitive unit cell of HfNCl has rhombohedral structure (space group $R\bar{3}m$, number 166) with 2 formula units per unit cell. It can also be constructed by a conventional cell of hexagonal structure with 6 formula units per cell with ABC stacking. Instead of using the rhombohedral unit cell, we take advantage of the weak interlayer interaction^{20,24,25,35,36}, which makes the stacking order negligible, and we adopt a hexagonal HfNCl structure with AAA stacking. This is equivalent to the hexagonal structure with the space group $P\bar{3}m1$ (space group number 164), with 2 formula units in the unit cell. We use the experimental lattice parameters a and c for each doping from Reference 15.

To confirm the assumption that the stacking order does not play a significant role in the conduction band, we compare the electronic bands and the density of states of hexagonal and rhombohedral structures for the doping $x = 0.11$ in Figure 1. The electronic structure is not affected by the stacking difference.

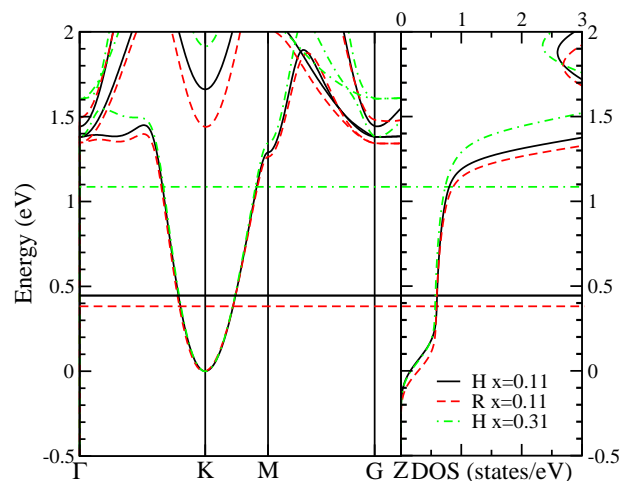


FIG. 1. Electronic structure and density of states (DOS) of Li_xHfNCl calculated with the PBE functional. The hexagonal structure (H) with AAA stacking is compared to the rhombohedral structure (R) with ABC stacking for the doping $x = 0.11$. For the hexagonal structure with AAA stacking, the electronic structure of the doping $x = 0.11$ is compared to that of the doping $x = 0.31$. The DOS is given in units of states/eV per 2 formula units of each unit cell.

This layered system can be considered as the prototype of 2D two-valley electron gas. Indeed the bottom of the conduction band of HfNCl is composed of two perfectly parabolic bands at points \mathbf{K} and $\mathbf{K}' = 2\mathbf{K}$ in the Brillouin zone. The conduction band is a simple parabola, with a minimum at the \mathbf{K} -point of the Brillouin zone. And the density of states is essentially constant along the parabolic part of the conduction band. The curvature of the rhombohedral structure is slightly smaller, hence the

Fermi energy is slightly lower, than the hexagonal structure. This difference also would lead to slightly larger effective mass calculated with the rhombohedral structure. The rest of the calculations are performed with the hexagonal structure.

Upon Li intercalation, Li atoms are placed between the HfNCl layers. Li acts as a donor and gives electrons to the Hf-N layers. The density of states stays almost constant as shown in our virtual crystal calculation for Li_xHfNCl in Figure 1. The semiconducting state is lost with doping and superconductivity emerges. While it is well-established that in Li_xZrNCl the superconducting state is enhanced at low doping^{9,10,14}, there is no evidence of this enhancement in experiments with Li_xHfNCl .

TABLE I. The fundamental band gap, E_g between the valence band maximum at the Γ point and the conduction band minimum at the \mathbf{K} point, effective mass, m^* , and density of states at the Fermi level, $N(0)$ of each doping calculated with the PBE and HSE06 functionals.

x	XC	E_g (eV)	m^* (m_e)	$N(0)$ (states/eV)
0	PBE	2.203	0.615	
0.055	PBE	2.195	0.599	0.587
0.11	PBE	2.171	0.585	0.632
0.13	PBE	2.168	0.580	0.639
0.16	PBE	2.164	0.572	0.654
0.18	PBE	2.156	0.568	0.666
0.20	PBE	2.153	0.564	0.680
0.31	PBE	2.130	0.540	0.833
0	HSE06	3.330	0.522	
0.055	HSE06	3.240	0.496	0.511
0.11	HSE06	3.148	0.472	0.539
0.13	HSE06	3.121	0.466	0.545
0.16	HSE06	3.084	0.456	0.556
0.18	HSE06	3.055	0.451	0.565
0.20	HSE06	3.031	0.446	0.577
0.31	HSE06	2.908	0.425	0.723

In Table I, we present the band gap, E_g , effective mass, m^* , and density of states, $N(0)$ of each doping with the PBE and HSE06 functionals. The band gap, E_g decreases with increased doping for both functionals. As the doping increases, the m^* decreases, and this trend is similar in ZrNCl ²⁶. However, in general, the effective mass of HfNCl is slightly larger than that of ZrNCl. Similarly, the $N(0)$ is larger in HfNCl than ZrNCl for all doping²⁶.

B. Spin susceptibility

Similar to the T_c , the magnetic spin susceptibility is enhanced in Li_xZrNCl at low doping^{37,38}, whereas there are no experiments of spin susceptibility as a function of doping for Li_xHfNCl . Spin susceptibility is the response of the spin magnetization to an applied magnetic field:

$$\chi_s = \left(\frac{\partial^2 E}{\partial M^2} \right)^{-1}, \quad (1)$$

where E and M are the total energy and magnetization, respectively. The non interacting spin susceptibility, χ_{0s} , is obtained by neglecting the electron-electron interaction of the conducting electrons. For perfectly parabolic bands, the non interacting spin susceptibility is doping independent and equal to

$$\chi_{0s} = \mu_s N(0) = \frac{g_v m^*}{\pi \hbar^2}, \quad (2)$$

where μ_s is the Bohr magneton, g_v is the valley degeneracy (2 in our case) and m^* the band effective mass. We calculate χ_{0s} from the density of states of the undoped compound, and by extrapolating the $N(0)$ of the desired doping. Our calculations show that χ_{0s} is not enhanced at the low-doping limit. As $N(0)$ is larger in HfNCl, the χ_{0s} is also larger in HfNCl than ZrNCl²⁶.

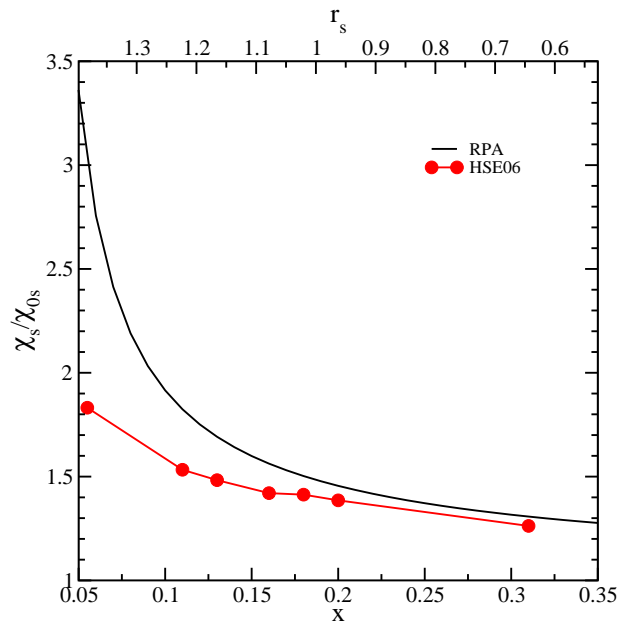


FIG. 2. Spin susceptibility enhancement at different doping with the RPA and HSE06 approximations.

We calculate the spin susceptibility with the HSE06 hybrid functional by calculating the total energy at fixed magnetization and then using equation 1 to obtain χ_s . We choose the HSE06 functional, because it can reproduce the χ_s/χ_{0s} of ZrNCl ²⁶. We also compare our results with those obtained by a model based on RPA^{25,39}. The model is appropriate in the low-doping limit where $|\mathbf{k}_F - \mathbf{K}| \ll K$, a condition necessary to have the intravalley electron-electron scattering dominating over the intervalley one, as explained in the supplementary material of Reference 25. This model assumes a 2D two-valley electron gas with no intervalley Coulomb scattering. Therefore, only the intravalley electron-electron interaction remains and the RPA susceptibility can be calculated analytically, by using the PBE effective mass of undoped HfNCl and the environmental dielectric constant, $\epsilon_M = 4.93$ ²¹. This value is smaller in HfNCl than ZrNCl ($\epsilon_M = 5.59$)²⁵.

In a 2D two-valley electron gas, the reduction of doping implies an increase of the r_s electron-gas parameter, and, consequently, of the electron-electron interaction⁴⁰. The effective mass of β -HfNCl as calculated by the PBE functional is larger ($0.615 m_e$) than β -ZrNCl ($0.57 m_e$ ²⁵). Therefore, both the larger m^* and the smaller ϵ_M of HfNCl lead to larger r_s as compared to ZrNCl, at similar low-doping regime²⁵. This implies that the electron-electron interaction is larger in HfNCl, and hence the spin susceptibility enhancement is also larger in HfNCl. While the spin susceptibility enhancement at low doping is present for both calculations with the RPA and the HSE06 functional, as presented in Figure 2, it is milder with the HSE06 functional than the RPA calculation.

C. Electron-phonon interaction

The electron-phonon coupling of a mode ν at a phonon-momentum \mathbf{q} is defined as

$$\tilde{\lambda}_{\mathbf{q}\nu} = \frac{2}{\omega_{\mathbf{q}\nu}^2 N(0) N_k} \sum_k |\tilde{d}_{\mathbf{k}, \mathbf{k}+\mathbf{q}}^\nu|^2 \delta(\epsilon_{\mathbf{k}}) \delta(\epsilon_{\mathbf{k}+\mathbf{q}}), \quad (3)$$

where $\epsilon_{\mathbf{k}}$ is the quasiparticle energy and the electron-phonon matrix elements are defined such that $\tilde{d}_{\mathbf{k}, \mathbf{k}+\mathbf{q}}^\nu = \langle \mathbf{k} | \delta \tilde{V} / \delta u_{\mathbf{q}\nu} | \mathbf{k} + \mathbf{q} \rangle$, $u_{\mathbf{q}\nu}$ is the phonon displacement of the mode $\omega_{\mathbf{q}\nu}$, and \tilde{V} is the single particle potential that is fully screened by charge, spin, and valley exchange and correlation effects (see Eq. 2 in Reference 25 for more details). We first calculate the non-interacting $\lambda_{\mathbf{q}\nu}$ with the PBE functional, that does not have the valley polarization dependence, using the Wannier interpolation method³⁴.

In Figure 3, we show the phonon dispersion along the high symmetry directions, and the Eliashberg function, $\alpha^2 F(\omega)$ and the electron-phonon coupling, $\lambda(\omega)$ for the doping $x = 0.055$. The Eliashberg function has two distinct peaks that are dominated by the modes with large phonon linewidths, $\gamma_{\mathbf{q}\nu}$ at the \mathbf{K} -point of the Brillouin zone at the energies ~ 19 meV and ~ 59 meV. To analyze the contribution to the electron-phonon coupling, we separate it into the inter- and intra-valley components. The intervalley electron-phonon coupling, λ^{inter} , is defined such that the modes contributing to the coupling are in the vicinity of the \mathbf{K} and $2\mathbf{K}$ points such that, in equation 3, $\mathbf{k} \in I(\mathbf{K})$ and $\mathbf{k} + \mathbf{q} \in I(2\mathbf{K})$; or $\mathbf{k} \in I(2\mathbf{K})$ and $\mathbf{k} + \mathbf{q} \in I(\mathbf{K})$. The rest of the coupling is attributed to the intravalley electron-phonon coupling, λ^{intra} . Also shown in Figure 3 that these modes at the \mathbf{K} -point contribute significantly to intervalley component of the Eliashberg function and have a large intervalley electron-phonon coupling λ^{inter} . Therefore, they induce a valley polarization in this system²⁵.

Consequently, the spin susceptibility enhancement is directly linked to the enhancement in the electron-phonon coupling due to the intervalley interaction^{25,26}. The intervalley electron-phonon coupling is enhanced

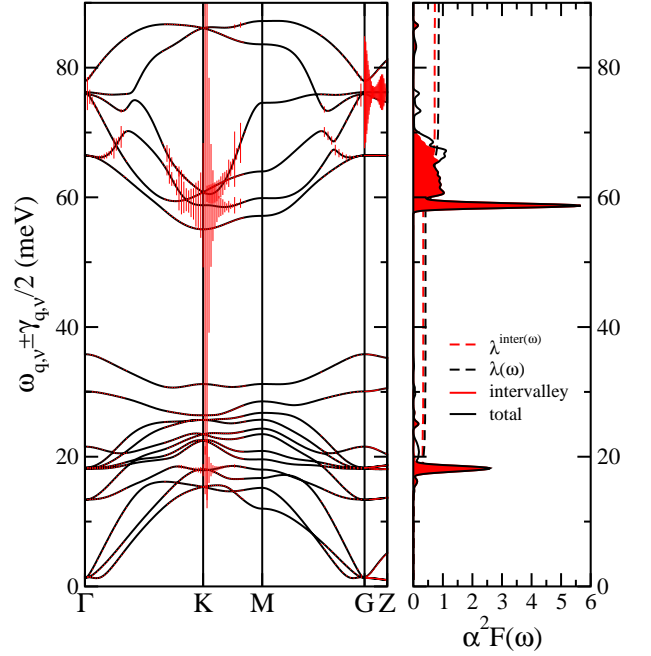


FIG. 3. Left: Phonon dispersion along the high symmetry directions of the Brillouin zone for $\text{Li}_{0.055}\text{HfNCl}$. Right: The total and intervalley component of the Eliashberg function, $\alpha^2 F(\omega)$ and the electron-phonon coupling, $\lambda(\omega)$.

similarly to χ_s/χ_{0s} such that

$$\frac{\tilde{\lambda}_{\mathbf{q}\nu}^{\text{inter}}}{\lambda_{\mathbf{q}\nu}^{\text{inter}}} = \left(\frac{\chi_s}{\chi_{0s}} \right)^2. \quad (4)$$

Following the previously developed methodology,^{25,26} we first calculate the bare intervalley electron-phonon coupling λ with the PBE functional, and use the spin susceptibility enhancement of RPA or HSE06 to obtain the corresponding fully dressed coupling $\tilde{\lambda}$.

In Table II, we present the bare electron-phonon coupling λ , and its intra- and inter-valley components, λ^{intra} , λ^{inter} calculated with the PBE functional, as well as the fully-interacting electron-phonon coupling for the RPA and the HSE06 calculations, $\tilde{\lambda}^{\text{RPA}}$, $\tilde{\lambda}^{\text{HSE06}}$ and their corresponding ω_{log} values.

D. Superconductivity and T_c enhancement

Finally, we calculate the superconducting critical temperature T_c using the McMillan-Allen-Dynes equation^{41,42}:

$$T_c = \frac{\omega_{\text{log}}}{1.20} \exp \left(-\frac{1.04(1 + \tilde{\lambda})}{\tilde{\lambda} - \mu^*(1 + 0.62\tilde{\lambda})} \right), \quad (5)$$

where $\mu^* = \mu/[1 + \mu \log(\epsilon_F/\omega_D)]$ is the screened Coulomb pseudopotential, with ϵ_F and $\omega_D = 900$ meV being Fermi and Debye energy respectively. We set the unscreened

TABLE II. For each doping, the bare electron-phonon coupling λ and its intravalley λ^{intra} and intervalley λ^{inter} components as calculated by the PBE functional; the fully-interacting electron-phonon coupling for the RPA and the HSE06 functionals, $\tilde{\lambda}^{\text{RPA}}$ and $\tilde{\lambda}^{\text{HSE06}}$; the PBE functional values of $\omega_{\text{log}}^{\text{PBE}}$ with the intra- and intervalley components, $\omega_{\text{log}}^{\text{PBEintra}}$ and $\omega_{\text{log}}^{\text{PBEinter}}$; and the rescaled $\omega_{\text{log}}^{\text{RPA}}$ and $\omega_{\text{log}}^{\text{HSE06}}$ in meV. The screened Coulomb pseudopotential μ^* and the T_c values calculated by the RPA and HSE06 functional are also given.

x	λ	λ^{intra}	λ^{inter}	$\tilde{\lambda}^{\text{RPA}}$	$\tilde{\lambda}^{\text{HSE06}}$	$\omega_{\text{log}}^{\text{PBE}}$	$\omega_{\text{log}}^{\text{PBEintra}}$	$\omega_{\text{log}}^{\text{PBEinter}}$	$\omega_{\text{log}}^{\text{RPA}}$	$\omega_{\text{log}}^{\text{HSE06}}$	μ^*	T_c^{RPA}	T_c^{HSE06}
0.055	0.861	0.133	0.728	6.730	2.578	34.219	28.494	35.385	35.233	34.991	0.326	68.60	39.39
0.11	0.789	0.167	0.622	2.236	1.628	32.593	28.285	33.854	33.404	33.235	0.276	38.15	25.18
0.13	0.803	0.182	0.621	1.959	1.547	31.458	27.882	32.588	32.120	31.997	0.266	32.97	23.36
0.16	0.860	0.208	0.652	1.800	1.523	28.643	26.451	29.380	29.026	28.962	0.254	28.17	21.86
0.18	0.889	0.225	0.664	1.724	1.551	26.781	25.103	27.373	27.066	27.032	0.248	25.69	21.67
0.20	0.932	0.256	0.676	1.688	1.554	26.370	24.686	27.040	26.668	26.636	0.242	24.81	21.96
0.31	0.973	0.372	0.601	1.401	1.331	25.915	25.956	25.887	25.905	25.906	0.222	19.89	18.30

$\mu = 0.231$ that gives the correct estimate of the experimental $T_c = 19.94$ K at the highest doping of $x = 0.31$ by using the RPA enhanced fully screened electron-phonon coupling, $\tilde{\lambda}$. This is in agreement with the GW estimate of $\mu = 0.237$ at $x = 0.1^{22}$. We present the screened Coulomb pseudopotential, μ^* that is used to calculate the T_c for each doping and the final T_c values for the RPA and HSE06 calculations in Table II.

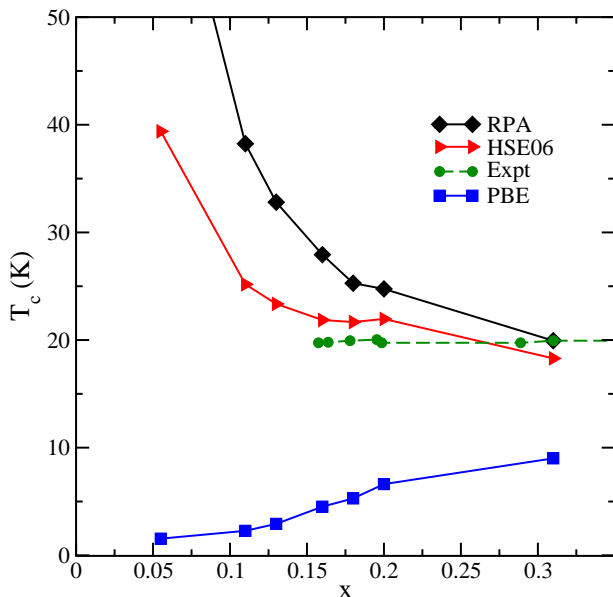


FIG. 4. Superconducting critical temperature T_c as a function of doping calculated with the bare electron-phonon coupling, $\lambda_{\mathbf{q}\nu}$ as calculated by the PBE functional, and with the fully dressed electron-phonon coupling, $\tilde{\lambda}_{\mathbf{q}\nu}$ using the RPA and HSE06 functional. The experimental data is taken from Reference 15.

With the PBE functional, the superconducting temperature, T_c is reduced in the low-doping limit, in stark disagreement with experiments, as shown in Figure 4. When the dressing of the intervalley electron-phonon coupling by the intravalley Coulomb interaction is taken into account, the T_c is enhanced in a similar fashion of what happens to the spin susceptibility, i.e. it is en-

hanced significantly, up to ~ 70 K, with RPA, while the enhancement is softer, up to ~ 40 K with the HSE06 functional. In addition, the HSE06 functional agrees well with the experimental T_c for the doping between $0.15 < x < 0.20$. We show the details of this scaling for the RPA calculation in A, and we present the phonon dispersion, ω , Eliashberg function $\alpha^2 F(\omega)$, and electron-phonon coupling $\lambda(\omega)$ for the rest of the dopings in B.

IV. CONCLUSION

We study the electronic, magnetic, and vibrational properties of Li_xHfNCl at the low-doping regime. We first calculate the electronic structure and find that the effective mass m^* and the density of states, $N(0)$ are larger in HfNCl as compared to ZrNCl, both for the PBE and the HSE06 functionals.

As there are no experimental data for the spin susceptibility of HfNCl as a function of doping, we calculate the spin susceptibility enhancement using both RPA calculations and the HSE06 functional. Both m^* and ϵ_M contribute to a larger r_s in HfNCl than ZrNCl. Therefore, the spin susceptibility enhancement is larger in HfNCl than ZrNCl at the low-doping limit and this is visible both in the RPA calculations and the HSE06 calculations of χ_s/χ_{0s} .

Then, we calculate the phonon dispersion $\omega_{\mathbf{q}\nu}$, Eliashberg function $\alpha^2 F(\omega)$, and the bare electron-phonon coupling $\lambda(\omega)$ using the PBE functional. We further calculate the fully-dressed electron-phonon coupling $\tilde{\lambda}$, based on the enhancement in the spin susceptibility.

This enhancement is then directly reflected in the calculated T_c . There is no enhancement in the T_c with the PBE functional. On the other hand, we can speculate that depending on the enhancement in the spin susceptibility, high T_c , can be reached; ranging from 40 K (with the HSE06 functional) to 70 K (with the RPA calculation). Furthermore, the HSE06 functional gives comparable T_c values to the experiments for dopings $0.15 < x < 0.20$. However, the T_c goes to zero in experiments for the reported doping $x < 0.15^{15}$. A possible explanation for this disagreement is that the disorder at

the low-doping limit can lead to Anderson localization. Alternatively, it could be that the reported doping is only a nominal doping. Experiments of field-effect doping can also help to learn more about the low-doping regime. In either case, our results predict that removal of the Anderson transition or better control of doping in Li_xHfNCl could lead to emergence of a high T_c superconducting state.

ACKNOWLEDGMENTS

This project has received funding from the European Union's Horizon 2020 research and innovation programme under Grant Agreement 696656 GrapheneCore1. Calculations were performed at Marenostrum, IDRIS, CINES, CEA, BSC TGCC and institute for computing and data sciences (ISCD) at UPMC. We acknowledge PRACE for awarding us access to resource Marenostrum based in Spain. B. P. acknowledges National Science Foundation (Platform for the Accelerated Realization, Analysis, and Discovery of Interface Materials (PARADIM)) under Cooperative Agreement No. DMR-1539918 for her time at Cornell University.

Appendix A: Electron-phonon Coupling Scaling

We present the electron-phonon coupling in equation 5 as a function of doping in Figure 5. The top panel shows the average non-interacting electron-phonon coupling λ , as well as the inter- and intra-valley components of it.

The second panel shows the total ω_{\log} , also decomposed into inter- and intra-valley components. In addition, we also present how it is rescaled with the RPA calculation, by rescaling of the $\tilde{\lambda}_{\text{inter}}$. Starting with the definition of ω_{\log} :

$$\omega_{\log} = \exp \left[\frac{2}{\lambda} \int_0^{+\infty} \alpha^2 F(\omega) \frac{\log(\omega)}{\omega} d\omega \right], \quad (\text{A1})$$

we have separated ω_{\log} into inter- and intra-valley terms. The inter-valley term is

$$\omega_{\log}^{\text{inter}} = \exp \left[\frac{2}{\lambda_{\text{inter}}} \int_0^{+\infty} \alpha^2 F(\omega)^{\text{inter}} \frac{\log(\omega)}{\omega} d\omega \right], \quad (\text{A2})$$

and intra-valley term is defined similarly. The relation between these two terms hold such that

$$\omega_{\log} = (\omega_{\log}^{\text{inter}})^{\lambda^{\text{inter}}/\lambda} \times (\omega_{\log}^{\text{intra}})^{\lambda^{\text{intra}}/\lambda}. \quad (\text{A3})$$

Therefore, we rescaled it for the RPA calculation by keeping the intravalley λ^{intra} component the same, but rescaling the full-interacting intervalley $\tilde{\lambda}^{\text{inter}}$ and hence the total $\tilde{\lambda}$ electron-phonon coupling elements. These are shown in the third panel of the figure for the RPA calculations.

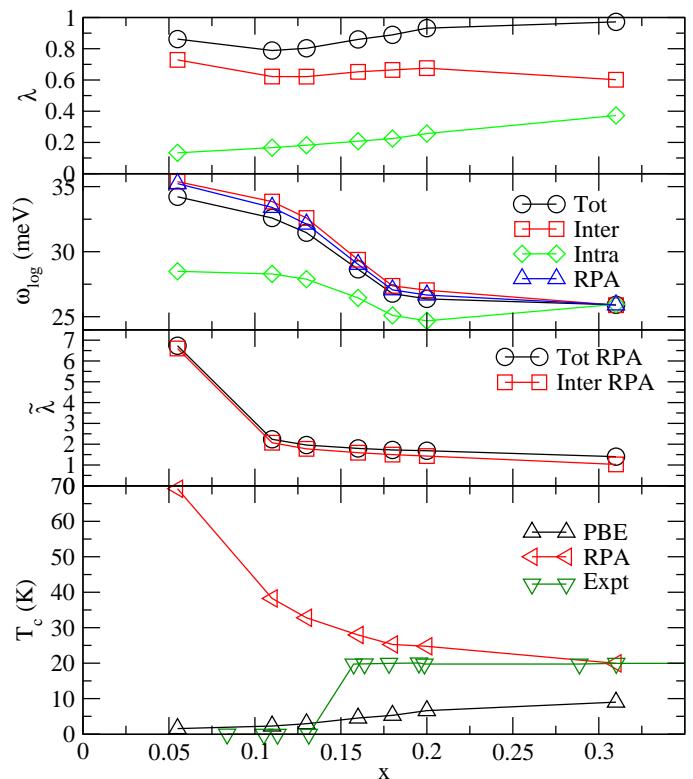


FIG. 5. First panel: Average non-interacting electron-phonon coupling λ for each doping including the inter- and intra-valley components as calculated with the PBE functional. Second panel: ω_{\log} for each doping with inter- and intra-valley components, as well as rescaled $\omega_{\log}^{\text{RPA}}$. Third panel: The interacting electron-phonon coupling $\tilde{\lambda}$ where the inter-valley term is rescaled with by RPA electron-electron interaction enhancement. Fourth panel: Superconducting critical temperature T_c as a function of doping, calculated by non-interacting (PBE) and interacting (RPA) electron-phonon coupling, as compared to the experiments from Reference 15.

For completeness, we also present the final calculated T_c without the intervalley enhancement using the PBE functional, and with the intervalley enhancement using the RPA calculation, similar to the Figure 4.

Appendix B: Phonon Modes as a Function of Doping

In this section, we present the phonon dispersion of Li_xHfNCl for all doping values. The left panels of Figure 6 show the phonon dispersion with increasing doping. Similarly the right panels show the corresponding Eliashberg function, $\alpha^2 F(\omega)$ and the electron-phonon coupling $\lambda(\omega)$. In all cases, there are two distinct peaks of $\alpha^2 F(\omega)$, and consequently an increase in the $\lambda(\omega)$.

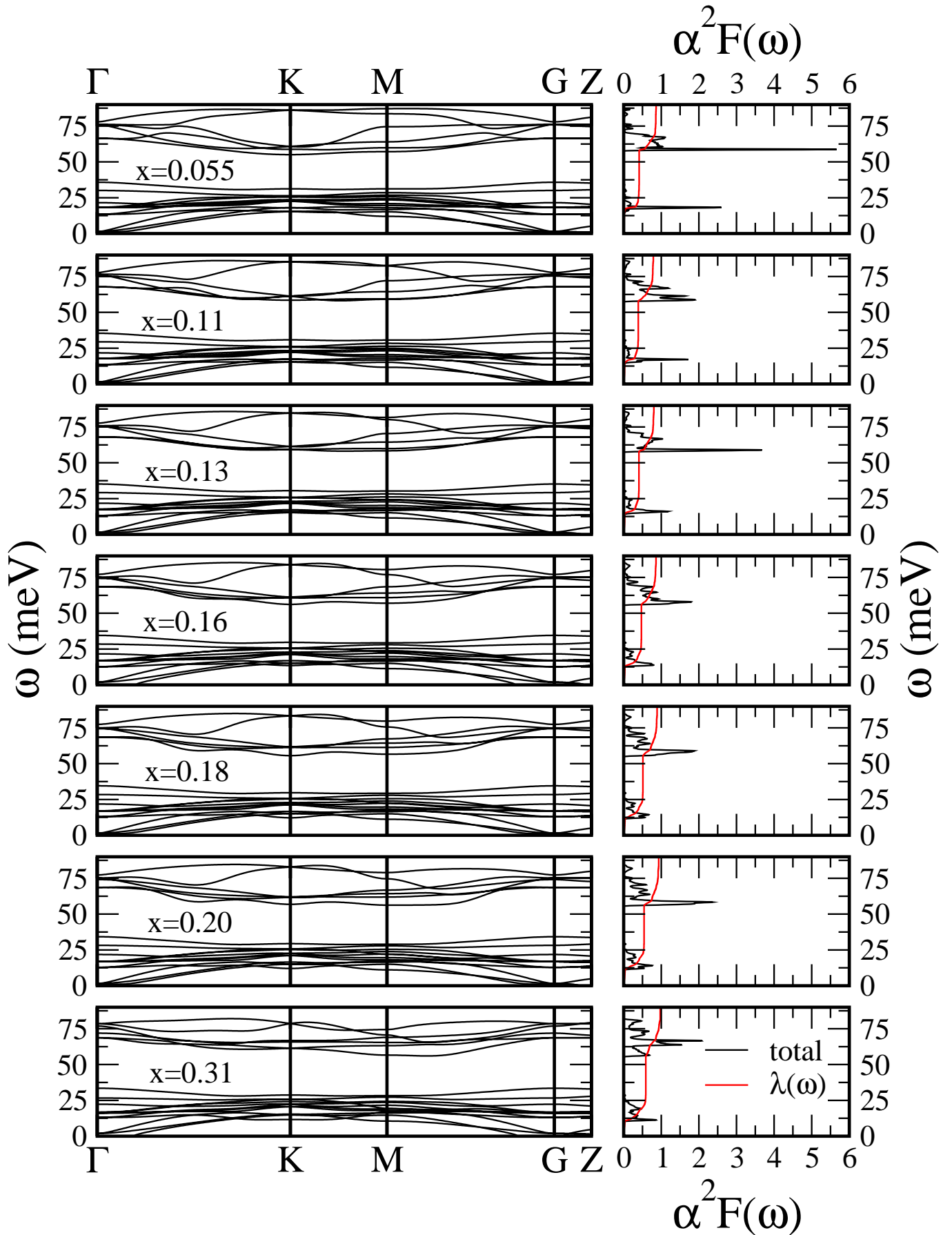


FIG. 6. Left: Phonon dispersion of Li_xHfNCl as a function of doping. Right: Total Eliashberg function, $\alpha^2 F(\omega)$ and electron phonon coupling, $\lambda(\omega)$

- * francesco.mauri@uniroma1.it
† matteo.calandra@upmc.fr
- ¹ Y. Saito, Y. Kasahara, J. Ye, Y. Iwasa, and T. Nojima, *Science* **350**, 409 (2015).
 - ² J. M. Lu, O. Zheliuk, I. Leermakers, N. F. Q. Yuan, U. Zeitler, K. T. Law, and J. T. Ye, *Science* **350**, 1353 (2015).
 - ³ Y. Kasahara, K. Kuroki, S. Yamanaka, and Y. Taguchi, *Physica C: Superconductivity and its Applications* **514**, 354 (2015).
 - ⁴ K. S. Novoselov, D. Jiang, F. Schedin, T. J. Booth, V. Khotkevich, S. V. Morozov, and A. K. Geim, *Proc. Nat. Acc. Sci.* **102**, 10451 (2005).
 - ⁵ X. Xu, W. Yao, D. Xiao, and T.-F. Heinz, *Nat. Phys.* **10**, 343 (2014).
 - ⁶ Y. J. Zhang, T. Oka, R. Suzuki, J. T. Ye, and Y. Iwasa, *Science* **344**, 725 (2014).
 - ⁷ J. T. Ye, Y. J. Zhang, R. Akashi, M. S. Bahramy, R. Arita, and Y. Iwasa, *Science* **338**, 1193 (2012).
 - ⁸ D. Gregory, M. Barker, P. Edwards, M. Slaskic, and D. Siddonsa, *J. Solid State Chem.* **137**, 62 (1998).
 - ⁹ S. Yamanaka, H. Kawaji, K. i. Hotehama, and M. Ohashi, *Adv. Mater.* **8**, 771 (1996).
 - ¹⁰ S. Yamanaka, K. Hotehama, and H. Kawaji, *Nature (London)* **392**, 580 (1998).
 - ¹¹ J. T. Ye, S. Inoue, K. Kobayashi, Y. Kasahara, H. T. Yuan, H. Shimotani, and Y. Iwasa, *Nat. Mater.* **9**, 125 (2010).
 - ¹² Y. Kasahara, T. Nishijima, T. Sato, Y. Takeuchi, J. Ye, H. Yuan, H. Shimotani, and Y. Iwasa, *J. Phys. Soc. Jpn.* **80**, 023708 (2011).
 - ¹³ T. Brumme, M. Calandra, and F. Mauri, *Phys. Rev. B* **89**, 245406 (2014).
 - ¹⁴ Y. Taguchi, A. Kitora, and Y. Iwasa, *Phys. Rev. Lett.* **97**, 107001 (2006).
 - ¹⁵ T. Takano, T. Kishiume, Y. Taguchi, and Y. Iwasa, *Phys. Rev. Lett.* **100**, 247005 (2008).
 - ¹⁶ T. Takano, A. Kitora, Y. Taguchi, and Y. Iwasa, *Journal of Physics and Chemistry of Solids* **69**, 3089 (2008).
 - ¹⁷ S. Yamanaka, T. Yasunaga, K. Yamaguchi, and M. Tagawa, *J. Mater. Chem.* **19**, 2573 (2009).
 - ¹⁸ E. A. Ekimov, V. A. Sidorov, E. D. Bauer, N. N. Mel'nik, N. J. Curro, J. D. Thompson, and S. M. Stishov, *Nature (London)* **428**, 542 (2004).
 - ¹⁹ R. Weht, A. Filippetti, and W. E. Pickett, *Europhys. Lett.* **48**, 320 (1999).
 - ²⁰ R. Heid and K.-P. Bohnen, *Phys. Rev. B* **72**, 134527 (2005).
 - ²¹ A. Kaur, E. R. Ylvisaker, Y. Li, G. Galli, and W. E. Pickett, *Phys. Rev. B* **82**, 155125 (2010).
 - ²² R. Akashi, K. Nakamura, R. Arita, and M. Imada, *Phys. Rev. B* **86**, 054513 (2012).
 - ²³ Z. P. Yin, A. Kutepov, and G. Kotliar, *Phys. Rev. X* **3**, 021011 (2013).
 - ²⁴ A. S. Botana and W. E. Pickett, *Phys. Rev. B* **90**, 125145 (2014).
 - ²⁵ M. Calandra, P. Zocante, and F. Mauri, *Phys. Rev. Lett.* **114**, 077001 (2015).
 - ²⁶ B. Pamuk, J. Baima, R. Dovesi, M. Calandra, and F. Mauri, *Phys. Rev. B* **94**, 035101 (2016).
 - ²⁷ P. Giannozzi, S. Baroni, N. Bonini, M. Calandra, R. Car, C. Cavazzoni, D. Ceresoli, G. L. Chiarotti, M. Cococcioni, I. Dabo, A. Dal Corso, S. de Gironcoli, S. Fabris, G. Fratesi, R. Gebauer, U. Gerstmann, C. Gougousis, A. Kokalj, M. Lazzeri, L. Martin-Samos, N. Marzari, F. Mauri, R. Mazzarello, S. Paolini, A. Pasquarello, L. Paulatto, C. Sbraccia, S. Scandolo, G. Sclauzero, A. P. Seitsonen, A. Smogunov, P. Umari, and R. M. Wentzcovitch, *J. Phys. Condens. Matter* **21**, 395502 (2009).
 - ²⁸ J. P. Perdew, K. Burke, and M. Ernzerhof, *Phys. Rev. Lett.* **77**, 3865 (1996).
 - ²⁹ A. V. Krukau, O. A. Vydrov, A. F. Izmaylov, and G. E. Scuseria, *J. Chem. Phys.* **125**, 224106 (2006).
 - ³⁰ R. Dovesi, R. Orlando, A. Erba, C. M. Zicovich-Wilson, B. Civalieri, S. Casassa, L. Maschio, M. Ferrabone, M. D. L. Pierre, P. D'Arco, Y. Noël, M. Causà, M. Rérat, and B. Kirtman, *Int. J. Quantum Chem.* **114**, 1287 (2014).
 - ³¹ F. Weigend and R. Ahlrichs, *Phys. Chem. Chem. Phys.* **7**, 3297 (2005).
 - ³² D. Muñoz Ramo, J. L. Gavartin, A. L. Shluger, and G. Bersuker, *Phys. Rev. B* **75**, 205336 (2007).
 - ³³ A. A. Mostofi, J. R. Yates, G. Pizzi, Y.-S. Lee, I. Souza, D. Vanderbilt, and N. Marzari, *Computer Physics Communications* **185**, 2309 (2014).
 - ³⁴ M. Calandra, G. Profeta, and F. Mauri, *Phys. Rev. B* **82**, 165111 (2010).
 - ³⁵ Y. Kasahara, T. Kishiume, K. Kobayashi, Y. Taguchi, and Y. Iwasa, *Phys. Rev. B* **82**, 054504 (2010).
 - ³⁶ T. Takano, Y. Kasahara, T. Oguchi, I. Hase, Y. Taguchi, and Y. Iwasa, *J. Phys. Soc. Jpn.* **80**, 023702 (2011).
 - ³⁷ Y. Kasahara, T. Kishiume, T. Takano, K. Kobayashi, E. Matsuoka, H. Onodera, K. Kuroki, Y. Taguchi, and Y. Iwasa, *Phys. Rev. Lett.* **103**, 077004 (2009).
 - ³⁸ Y. Taguchi, Y. Kasahara, T. Kishiume, T. Takano, K. Kobayashi, E. Matsuoka, H. Onodera, K. Kuroki, and Y. Iwasa, *Physica C: Superconductivity* **470**, S598 (2010).
 - ³⁹ Y. Zhang and S. Das Sarma, *Phys. Rev. B* **72**, 075308 (2005).
 - ⁴⁰ G. F. Giuliani and G. Vignale, *Quantum Theory of the Electron Liquid* (Cambridge, 2005).
 - ⁴¹ W. L. McMillan, *Phys. Rev.* **167**, 331 (1968).
 - ⁴² P. B. Allen and R. C. Dynes, *Phys. Rev. B* **12**, 905 (1975).